The role of gravitational instabilities, density structure and extension rate in the evolution of continental margins

E. BUROV

Laboratory of Tectonics UMR 7072, University of Pierre and Marie Curie, Paris, France

Abstract: Formation of rifted continental margins is associated with localized thinning and breakup of the continental lithosphere, driven or accompanied by the ascent of the lithosphere–asthenosphere boundary. Thinning creates sharp density and viscosity contrasts and steep boundaries between cold deformed lithosphere and hot upwelling asthenosphere, thus providing conditions for the development of positive (asthenosphere) and negative (mantle lithosphere) Rayleigh–Taylor (RT) instabilities. The evolution of many continental margins (e.g. Newfoundland margin and Iberian margin) is characterized by slow spreading rates. This allows the RT instabilities to grow at the timescale of rifting. The impact of positive RT instabilities (asthenospheric upwelling) is well studied. The negative RT instabilities, associated with mantle downwelling, remain an overlooked factor. However, these instabilities should also affect the rift evolution, in particular, they may cause mantle thinning or thickening below the rift flanks. Our numerical experiments suggest that the ratio of the RT-growth rate to the extension rate controls the overall rift geometry and evolution. Even if the effect of negative RT instabilities is more important for slow extension rates of 2×5 mm year^{-1} (Deborah number, $De < 1$), it is still significant for 2–3 times higher extension rates of 2×15 mm year^{-1} ($De < 10$). The numerical experiments for extension rates of 2×15 mm year^{-1} and mantle–asthenosphere density contrasts of 10–20 kg m^{-3} demonstrate a number of structural similarities with continental margins characterized by low De (e.g. Flemish Cap and Galicia margin). In particular, rift asymmetry results from interplay between the RT instabilities and differential stretching at $De < 1$. Formation of interior basins occurs at $De \approx 1$–3. The best correspondence with the observed geometry of rifted margins is obtained for chemical density contrast of 20 kg m^{-3} and extension rate of 2×15 mm year^{-1}, which is twice that of the averaged values inferred from the observations. This suggests that margins may initially (prebreakup stage) extend at higher rates than the average extension rates characterizing rift evolution. The influence of RT instabilities is strongly controlled by extension rate, density, rheology and thermal structure of the lithosphere; this implies that we need better constraints on these parameters from the observations.

Continental margins result from rifting characterized by large coefficients of extension $4–5 < \beta < 15$ (e.g. Bott 1971; Salvenson 1978; Cloetingh *et al.* 1982; Buck 1991). Rifting processes involve laterally variable thinning of ductile layers of different densities. If a denser layer (mantle lithosphere) is located on top of a lighter layer (asthenosphere), then the system is gravitationally unstable and may develop negative Rayleigh–Taylor (RT) instabilities. This possibility specifically refers to rifting, passive or active, where hot light asthenosphere ascends to the surface and replaces colder denser lithosphere. In most situations, normal lithospheric mantle is approximately 10–30 kg m^{-3} denser than the underlying asthenospheric layer, basically due to its colder temperature but also due to compositional differences (e.g. Stacey 1992; O'Reilly *et al.* 2001; Poudjom Djomani *et al.* 2001; Turcotte & Schubert 2002). Some authors (e.g. Houseman *et al.* 1981) assume even much higher total density differences of up to 100 kg m^{-3}. The density differences of the order of 20 kg m^{-3} are commonly accepted for the Phanerozoic lithosphere, even though there is still a debate about whether it applies to the presumably Mg-rich and -depleted cratonic lithosphere. Irrespective, volumetric seismic velocities, which are generally considered as proxy for density, are systematically higher in the lithosphere mantle than in the asthenosphere. Depending on its viscosity the mantle lithosphere therefore has the potential to sink as the result of a RT instability (e.g. Houseman *et al.* 1981). The growth rate of the RT instabilities is directly proportional to the density contrast and inversely proportional to the thickness and the viscosity of the upper layer (if the viscosity of the lower layer is small). Depending on that, the instabilities may be rapid or slow compared to the tectonic deformation rates. In the first case, they will influence the rift evolution, but not in the second. The conditions when the RT instabilities are slow apply to the cases when the viscosity of the mantle lithosphere is higher than 10^{22} Pa s, when the density contrast between the lithosphere

From: KARNER, G. D., MANATSCHAL, G. & PINHEIRO, L. M. (eds) *Imaging, Mapping and Modelling Continental Lithosphere Extension and Breakup*. Geological Society, London, Special Publications, **282**, 139–156.
DOI: 10.1144/SP282.7 0305-8719/07/$15.00 © The Geological Society of London 2007.

and the asthenosphere is small, or when the interface between the mantle and the asthenosphere remains flat (e.g. Houseman & Molnar 1997). This applies to oceanic and continental plates at normal conditions that infer smooth boundaries and smooth vertical temperature profiles and practical absence of lateral heat transport (e.g. prerift geotherm in Fig. 1a).

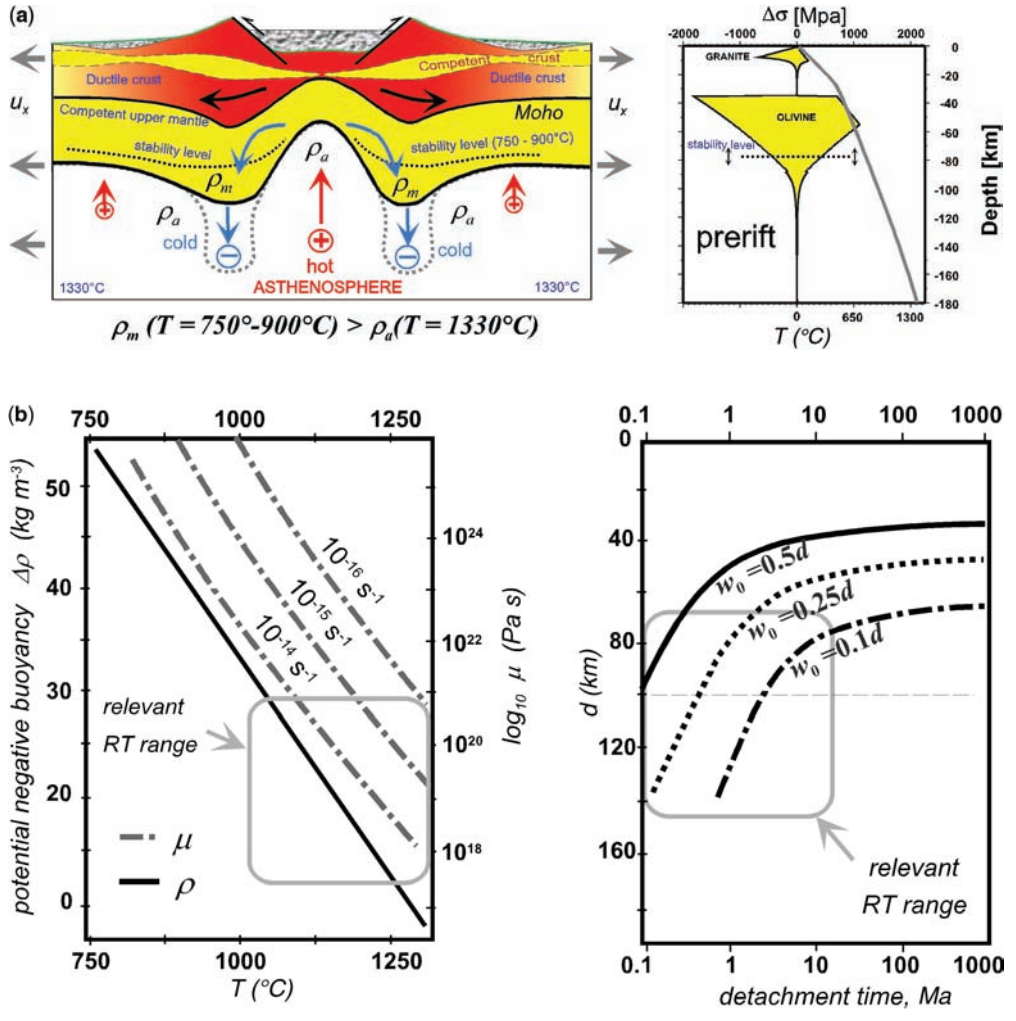


Fig. 1. (**a**) Simplified cartoon showing the interaction between the asthenosphere and mantle lithosphere during rifting. Left: the mantle lithosphere below the rift flanks becomes gravitationally unstable owing to the negative density contrast with the hot asthenosphere and the loss of mechanical resistance resulting from lateral heat transfer from the asthenosphere below the rifted zone. The asthenosphere is positively unstable because of its positive density contrast with the embedding mantle lithosphere. As the viscosity of the mantle lithosphere is exponentially dependent on temperature, there is a relatively net 'stability level' that separates the regions of high viscosity from thermally weakened regions of low viscosity. These regions are subject to development of rapid RT instabilities. Right: simplified yield-stress prerift envelope of the continental lithosphere and typical prerift temperature profile. (**b**) Left: potential density contrast (reference density at 750 °C) and viscosity of olivine mantle, as function of temperature (left). Viscosity is shown for three representative values of the background strain rate (10^{-14}, 10^{-15} and 10^{-16} s^{-1}). Right: time until full detachment of the unstable mantle layer, as a function of initial layer thickness (olivine rheology), computed according to Conrad & Molnar (1999). The initial perturbation amplitude is w_0. Note that for a normal depth–pressure–temperature profile of mantle lithosphere, the density contrast due to thermal expansion is nearly negated by the effect of compressibility (Turcotte & Schubert 2002). This is not the case of rifting when the mantle is heated without compensatory increase in pressure.

Contrary to normal lithosphere, the rifted margins such as the Newfoundland and Iberian margin (Manatshal & Bernoulli 1999; Manatshal *et al.* 2001; Funck *et al.* 2003; Pérez-Gussinyé *et al.* 2003; Hopper *et al.* 2004), as well as many 'common' continental rifts, constitute a perfect environment for development of gravitational instabilities owing to the presence of steep density boundaries and viscosity contrasts resulting from rifting (e.g. Huismans *et al.* 1998) (Fig. 1a). As mentioned above, most data suggest the existence of a compositional or chemical density contrast of $0-20\ \mathrm{kg\ m^{-3}}$ between the mantle lithosphere and asthenosphere (e.g. Stacey 1992; O'Reilly *et al.* 2001; Poudjom Djomani *et al.* 2001; Turcotte & Schubert 2002), except probably the cratonic mantle (our settings consider, however, a non-cratonic lithosphere).

In addition to potential chemical density contrasts, strong thermal density contrasts of $30-60\ \mathrm{kg\ m^{-3}}$ arise when the mantle–asthenosphere boundary is locally uplifted owing to the rifting. In this case, horizontal heat conduction becomes at least as important as the vertical heat conduction. For the temperature contrasts of $500-1000\ ^{\circ}\mathrm{C}$, associated with moderate coefficients of extension $\beta = 2-5$ (McKenzie 1978), horizontal thermal gradients may reach $10-20\ ^{\circ}\mathrm{C\ km^{-1}}$. The resulting lateral heat flow is of the order of $30-60\ \mathrm{mW\ m^{-2}}$, which is higher than the normal mantle heat flow ($30\ \mathrm{mW\ m^{-2}}$: Jaupart & Marschal 1999; Turcotte & Schubert 2002). The consequences of the lateral heat transfer on the density structure during the rifting has been extensively studied in previous literature (e.g. Royden & Keen 1980; Stephenson *et al.* 1989). These studies have provided a number of important corrections to the most common one-dimensional (1D) thermal subsidence models (McKenzie 1978). The thermo-mechanical consequences of the lateral heat exchanges were also investigated (e.g. Keen & Boutilier 1995), yet mainly in terms of their impact on the mantle viscosity and on the development of positive asthenosphere instabilities under the rift axis (transition from passive to active rifting, post-rift doming). In particular, Huismans *et al.* (1998) conducted a detailed study of differential stretching of inelastic lithosphere in terms of its interaction with the unstable asthenosphere. Yet, the negative mantle instabilities were beyond the scope of this model because the experiments of Huismans *et al.* (1998) were limited to the upper 120 km of the lithosphere instead of at least 250 km needed to account for the mantle RT instabilities below the rift flanks.

The asthenosphere has a low viscosity (5×10^{19} Pa s) and can flow at timescales of 1 ka. The associated heat advection is instantaneous compared to the rifting timescales that exceed 0.1–1 Ma. For $\beta = 2$, the temperature of the asthenospheric material advected to a depth of 70–90 km below the stretched lithosphere is around 1330 °C. The temperature of the prerift mantle lithosphere at this depth is only 750–800 °C (e.g. Kirby & Kronenberg 1987), (Fig. 1a). Consequently, even for a moderate extension, the temperature contrast, ΔT, between the upraised asthenosphere and the surrounding mantle lithosphere is around 500–600 °C. The associated thermal density contrast, $\Delta\rho_t$, is $50-60\ \mathrm{kg\ m^{-3}}$ ($\Delta\rho_t = \rho_0\alpha\Delta T$, where $\rho_0 = 3330\ \mathrm{kg\ m^{-3}}$ and $\alpha = 3 \times 10^{-5}\ \mathrm{K^{-1}}$). $\Delta\rho_t$ sums up with the chemical density contrast $\Delta\rho_c$ of $10-20\ \mathrm{kg\ m^{-3}}$ yielding important 'available negative buoyancy' (Conrad & Molnar 1999). The total density contrast may be 2–3 times higher than the contrast of $10-20\ \mathrm{kg\ m^{-3}}$ that is sufficient to drive mantle instabilities at time scales of 2–10 Ma (Conrad & Molnar 1999). Of course, the initially higher density contrast vanishes as the heat propagates from the upwelling asthenosphere to the mantle lithosphere. This decrease in density contrast slows down the RT instability. Yet, as the temperature rises, the mantle viscosity decreases. The reduction of viscosity, in contrast to that of density, accelerates the RT instability. Hence, the impact of lateral heat propagation on the growth rate of instability depends on the ratio of the density change rate, $\partial\rho(T)/\partial T$, to the viscosity change rate, $\partial\mu(T)/\partial T$. The density change rate $\partial\rho(T)/\partial T$ is linearly proportional to temperature: $\partial\rho(T)/\partial T = \alpha\rho$, where α is the coefficient of thermal expansion ($\alpha = 3 \times 10^{-5}\ \mathrm{K^{-1}}$). The viscosity change rate is super-exponential: for dislocation creep, $\mu(T) = \mu_0\exp(Q/nRT)$, from where $\partial\mu(T)/\partial T = -\mu_0 Q(nRT^2)^{-1}\exp(Q/nRT)$, where Q is activation enthalpy ($\approx 5 \times 10^5\ \mathrm{J\ mol^{-1}}$), $n \approx 3$ and R is the universal gas constant (see Table 2). A 200 °C temperature rise from 750 to 800 °C (mechanical bottom of the lithosphere: Kirby *et al.* 1987) reduces the initial density contrast between the mantle and asthenosphere by $20\ \mathrm{kg\ m^{-3}}$ (Turcotte & Schubert 2002). Yet, this temperature rise also reduces the effective viscosity by factor of 10^4 (!). Such reduction is sufficient to bring the system from a mechanically stable state ($\mu = 10^{23}-10^{24}$ Pa s) to an extremely unstable state at $\mu = 10^{19}-10^{20}$ Pa s (e.g. Conrad & Molnar 1999). Consequently, temperature rise in the mantle near the lithosphere–asthenosphere boundary will accelerate the growth rate of RT instability rather then reduce it.

The question on the significance of the negative RT instabilities for slow rifting is naturally related to the problem of possible variation of the extension rate during the rifting phase. The extension rates deduced for many rift systems are averaged over some important time spans. Yet, the mechanical

response of the brittle–ductile lithosphere depends on the strain rate at each moment of time. If the extension rate changes during the active phase of rifting, the final rift structures may differ even for similar amounts of extension.

No doubt, there is a large number of other factors that may crucially influence the evolution of rifted margins. In particular, inherited structures, heterogeneities, rheology or surface processes are certainly of great importance. Yet, their influence is well studied and discussed in the previous work (e.g. Kusznir & Karner 1985; Dunbar & Sawyer 1988; Bassi 1995; Burov & Cloetingh 1997; Huismans & Beaumont 2007). We thus focus our study on more overlooked factors: negative gravitational stabilities and initial density structure of the lithosphere.

Theoretical background

A number of studies (e.g. Houseman *et al.* 1981; Fletcher & Hallet 1983; Bassi & Bonnin 1988; Houseman & Molnar 1997; Huismans *et al.* 1998) have investigated the development of RT instabilities in normal, extended or shortened continental lithosphere as a function of thermo-rheological parameters. Based on these studies, the first-order condition for instable behaviour is formulated as:

$$\Delta\rho g d/2\tau_{\max} < d/d_{\text{fold}}$$

where $\Delta\rho$ is the density contrast between the mantle and the asthenosphere, g is the acceleration due to gravity, d is the thickness of the lithosphere, $\tau_{\max}$ is its maximal mechanical strength and d_{fold} is the characteristic decay length of ductile strength/viscosity. For mantle lithosphere (olivine) d/d_{fold} is around 10 and $\Delta\rho g d/2\tau_{\max}$ is negative or smaller than 3 (Fletcher & Hallet 1983; Bassi & Bonnin 1988). This indicates that the mantle lithosphere is instable and may need only a small perturbation to develop a gravitational instability. Rifting produces a very strong perturbation of the mantle–asthenosphere interface and increases density contrasts, thus almost inevitably leading to unstable behaviour of the mantle layer.

The results of simple linear analysis demonstrate that the growth rate of instability is mainly controlled by the density contrast and the viscosity of the mantle lithosphere (Chandrasekhar 1961; Fletcher & Hallet 1983). Let us first consider a simplified case of a layer of Newtonian fluid with viscosity μ, density ρ_m and thickness d placed on top of a weak fluid layer (asthenosphere) of lower density ρ_a. The growth rate $1/\tau$ of the developing instability w (vertical deflection of the layer) with initial amplitude w_0 depends on μ, on the wavelength of perturbation, λ, on the thickness of the layer, d, and on the density contrast, $\Delta\rho$ (Chandrasekhar 1961):

$$\begin{aligned} w &= w_0 \exp(t/\tau) \\ \tau &= 4\mu(\Delta\rho g d)^{-1}(\omega + (sh(\omega^{-1})ch(\omega^{-1}))^{-1}) \\ &\quad \times (\omega^2 th(\omega) - sh(\omega^{-1})ch(\omega^{-1}))^{-1} \end{aligned} \quad (1)$$

where $\omega = \lambda/2\pi d = (kd)^{-1}$, k is a wave number.

The most rapidly growing wavelength is $\lambda = 2.568d$, which corresponds to minimal growth time:

$$\tau_{\min} = 13.04\mu(\Delta\rho g d)^{-1}.$$

As can be seen, the growth time is directly proportional to the fluid viscosity; so that it is less than 1 Ma for viscosities of $\mu = 10^{20}$ Pa s (assuming $d = 100$ km and $\Delta\rho = 20$ kg m^{-3}, Fig. 1b). High ($>10^{22}$ Pa s) viscosity is needed to keep mantle layer quasi-stable for 10–15 Ma. For viscosities of the order of 10^{20}–10^{21} Pa s the mantle may be destabilized at timescales of 1–10 Ma that are perfectly compatible with typical timescales of continental rifting. The viscosity of $\mu = 10^{20}$ Pa s is usually attributed to the transition zone between the mantle and asthenosphere, which suggests that this zone can be instable.

A number of analytical studies have extended equation 1 to the cases of realistic non-linear rheologies (e.g. Conrad & Molnar 1999). These studies show that in the nonlinear case the growth rate is about n times higher than in the case of Newtonian rheology, where n is the power-law exponent n ($n = 3$ for most olivine rheologies). In the case of rifted continental lithosphere, a multitude of factors such as the rheological stratification and rift geometry affect the viscosity, temperature and the growth rate of instability (Fig. 1a, which justifies the numerical approach developed in this study). For example, as the lithosphere thins, d decreases and as a result the growth rate and wavelength of new instabilities might decrease too. However, thinning results in heating of the mantle layer. Consequently, the effect of thinning on the growth rate is mitigated owing to temperature-induced viscosity drop.

The importance of RT instabilities during rift development can be characterized by the ratio of the characteristic growth time of the instability to the characteristic time of the rifting phase, t_r, expressed by means of Deborah number, De:

$$De = \tau_{\min}/t_r = 13.04\mu/(\Delta\rho g d t_r).$$

If $De \gg 1$ the instabilities do not effect rift evolution. If $De \leq 1$ rift evolution is highly affected

by RT instabilities. A more conventional way to define *De* would be to set it as a ratio of the Maxwell relaxation time τ_m to flow time. Yet, in our case, the development of gravitational instabilities appears to be a leading process, which becomes clear from an estimate of the ratio of τ_{min} to τ_m:

$$\tau_{min}/\tau_m \approx 13G/\Delta\rho gd \approx 5E/\Delta\rho gd$$

where G is the elastic shear modulus and E is the Young modulus. $E \approx 2.5G$. For typical rocks $E \approx 10^{11}$ Pa. Thus, for all plausible values of $\Delta\rho gd$ ($\Delta\rho gd < 10-100$ MPa), τ_{min}/τ_m varies from 1000 to 10 000. Hence, gravitational instabilities must be a leading long-term process and Maxwell relaxation is of secondary importance.

Time of rifting, t_r, can be expressed as:

$$t_r = L/u_x$$

where L is the width of the rift and u_x is the rate of extension. Consequently,

$$De = 13.04\mu u_x/(\Delta\rho gdL). \quad (2)$$

We can further introduce the effective viscosity for ductile creep law:

$$\mu_{eff} = e_{\|}^{d(1-n)/n}(A^*)^{-1/n}\exp(H/nRT)$$

where $e_{\|}^d = \mathrm{Inv}_{\|}(e_{ij}))^{1/2}$ is the effective strain rate and $A^* = 1/2A \cdot 3^{(n+1)/2}$ is the material constant, H is the activation enthalpy, R is the gas constant and n is the power-law exponent. So that:

$$\mu_{eff} = \mu_0 \exp(H/nRT) \quad (3)$$

with

$$\mu_0 = e_{\|}^{d(1-n)/n}(A^*)^{-1/n}.$$

Taking into account the thermal dependency of density and viscosity, *De* becomes:

$$De = 13.04\,\mu_0 \exp(H/nRT)u_x/((\Delta\rho_c + \alpha\rho_0\Delta T)gdL) \quad (4)$$

where $\Delta\rho_c + \alpha\rho_0\Delta T = \Delta\rho$, $\Delta\rho_c$ is the compositional density contrast, α is the coefficient of thermal expansion, ρ_0 is the density at reference temperature and ΔT is the temperature change in respect to the reference temperature. Expression 4 indicates that slow extension rates enhance the impact of the gravity-driven instabilities, whereas fast spreading rates reduce them. This clearly suggests that slow extension favours instabilities and, as a natural consequence, rift asymmetry.

Numerical model

We conducted a series of numerical experiments to test the stability of the extending lithosphere as a function of the extension rate, density and thermo-rheological structure. In these experiments we introduced a lithospheric plate composed of crustal, mantle and asthenospheric rheological layers with brittle–ductile–elastic properties inferred from rock mechanics data (Tables 1 and 2). The model area (Fig. 2) is 500 km wide and 300 km deep (250 × 150 grid elements); the sub-Moho (35 km depth) lithospheric mantle has a thickness of 120 km, with thickness of the strong mechanical core of about 70–80 km (Fig. 1a).

Table 1. *Notations and physical values common for all experiments (Turcotte & Schubert 2002)*

Parameter	Values and units	Definition
σ, τ	Pa, MPa	Stress
P	Pa, MPa	Pressure
$\mathbf{u}$	m s^{-1}, mm year^{-1}	Velocity vector
μ	10^{19}–10^{25} Pa s	Effective viscosity
$\dot{\varepsilon}$	s^{-1}	Strain rate
T	°C	Temperature
h_c	7 km/35 km	Moho depth
d	120 km	Thickness of mantle lithosphere
ρ_m	3330 kg m^{-3}	Reference mantle density
ρ_a	3310–3330 kg m^{-3}	Asthenosphere density
$\Delta\rho_c$	0–20 kg m^{-3}	Compositional density contrast
g	9.8 m s^{-2}	Acceleration due to gravity
C_p	10^3 J kg^{-1} °C^{-1}	Specific heat
ΔT	250 °C	Temperature contrast
α	3×10^{-5} °C^{-1}	Thermal expansion

Table 2. *Specific rheology and related thermal parameters. Compilation by Burov* et al. *(2001).* ρ *is density;* Q, n, A *are material-dependent parameters of ductile flow laws (Kirby & Kronenberg 1987; Kohlstedt* et al. *1995). Other parameters from Turcotte & Schubert (2002).*

Parameter	Value
All rocks	
λ, G Lamé elastic constants ($\lambda = G$)	30 GPa
ϕ friction angle (Mohr–Coulomb rheology)	30°
C_0 cohesion (Mohr–Coulomb rheology)	20 MPa
Specific upper and weak (quartz) lower crust properties	
ρ (upper crust)	2800 kg m^{-3}
n (power-law exponent)	2.4
A (power-law constant)	6.7×10^{-6} MPa^{-n} s^{-1}
Q (creep activation enthalpy)	1.56×10^5 kJ mol^{-1}
Specific strong middle–lower crust properties (diabase or basalt)	
ρ	2980 kg m^{-3}
n (power-law exponent)	3.4
A (power-law constant)	2×10^{-4} MPa^{-n} s^{-1}
Q (creep activation enthalpy)	2.6×10^5 kJ mol^{-1}
Specific mantle properties (olivine)	
ρ (lithosphere)	3330 kg m^{-3}
n (power-law exponent)	3
A (power-law constant)	1×10^4 MPa^{-n} s^{-1}
Q (creep activation enthalpy)	5.2×10^5 kJ mol^{-1}
Thermal model	
Surface temperature (0 km depth)	0 °C
Temperature at the bottom of thermal lithosphere	1330 °C
Thermal conductivity of crust, k	2.5 W m^{-1} $°C^{-1}$
Thermal conductivity of mantle, k	3.5 W m^{-1} $°C^{-1}$
Thermal diffusivity of mantle, χ	10^{-6} m^2 s^{-1}
Radiogenic heat production at surface, H_s	9.5×10^{-10} W kg^{-1}
Radiogenic heat production decay depth, h_r	10 km
Prerift thermotectonic age of the lithosphere, t_q	150 Ma

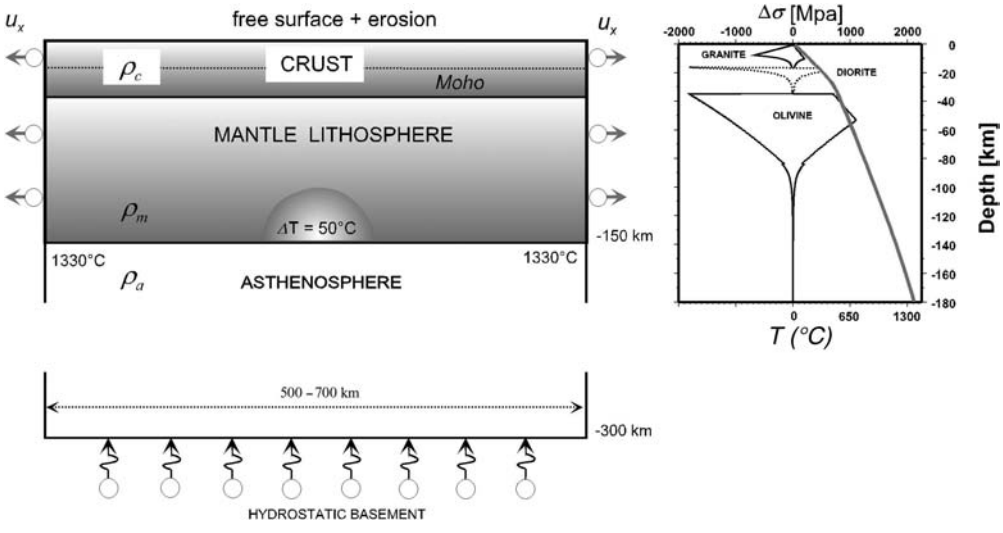


Fig. 2. Model set-up. The model box has dimensions of 500 × 300 km (250 × 150 grid elements). The initial rheology (explicit brittle–elastic–ductile) and temperature profile is shown on the right-hand side of the model. The initial weak temperature anomaly (+50 °C) is used to localize thinning in the middle of the model.

The boundary conditions are: (1) lateral velocities applied at the box sides; (2) free surface at the top of the model; and (3) restoring hydrostatic forces proportional to the vertical displacement at the basement. As pointed out by Huismans *et al.* (1998), whatever is the type of rifting (active or passive), the application of kinematic boundary conditions may be justified by the restricted size of the model. These conditions represent either far-field tectonic forces or the integrated effect of large-scale basal drag owing to the regional asthenospheric upwelling.

We use a 'generalized' initial geotherm that fits well the observed data for the Newfoundland–Galicia margin (Pérez-Gussinyé *et al.* 2001; Manatschal 2004). This geotherm provides 550 °C at Moho depth and 1330 °C at the base of the lithosphere, and falls in the middle of the interval between 400 °C at Moho depth (cratons) and 700 °C at Moho depth (young lithospheres) (e.g. Burov & Diament 1995). The localization of rifting in the middle of the model is achieved through the introduction of a small thermal anomaly (+50 °C) at the base of the mechanical lithosphere. This anomaly dissipates soon after the initiation of rifting and has no prolonged effect for the lateral stages of rift evolution.

The FLAC-like code Par(a)ovoz v9 (derived from Poliakov *et al.* 1993) solves the mechanical and thermal equilibrium equations in a large strain mode with no practical limitations on the imposed rheology laws because of its explicit time-marching scheme. The implementation and application of this algorithm to basin modelling is explained in detail in the abundant FLAC literature (Cundall 1989; Poliakov *et al.* 1993; Buck & Poliakov 1998; Lavier *et al.* 2000; Burov & Poliakov 2001, 2003; LePourhiet *et al.* 2004). For this reason, we limit its description to basic principals.

Par(a)ovoz is a large strain fully explicit time-marching Lagrangian algorithm that solves Newtonian equations of motion in the continuum mechanics approximation:

$$\langle \rho \dot{\mathbf{u}} \rangle - \mathrm{div}\sigma - \rho g = 0. \quad (5)$$

These equations are coupled with the constitutive equations of practically any kind:

$$\frac{D\sigma}{Dt} = F(\sigma, \mathbf{u}, \nabla\mathbf{u}, \ldots T \ldots), \quad (6)$$

and with the heat transport equations

$$\rho C_p \partial T/\partial t + \mathbf{u}\nabla T - k\,\mathrm{div}(\nabla T) - H_f = 0 \quad (7)$$

assuming adiabatic temperature dependency for density and a Boussinesq approximation for related body forces:

$$\rho = \rho_0(1 - \alpha\Delta T). \quad (8)$$

Here $\mathbf{u}$, σ, g, k are the respective terms for velocity, stress, acceleration due to body forces and thermal conductivity. The over-dots refer to the time derivatives. The brackets in equation 5 specify conditional use of the related term: in quasi-static mode, the inertia is dumped using inertial mass scaling (Cundall 1989). The terms t, ρ, C_p, T, H_r, α designate, respectively, time, density, specific heat, temperature, internal heat production and thermal expansion coefficient. The terms $\partial/\partial t$, $D\sigma/Dt$, F are a time derivative, an objective (Jaumann) stress time derivative and a functional, respectively. In the Lagrangian framework, the incremental displacements are added to the grid co-ordinates allowing the mesh to move and deform with the material. This enables solution of large-strain problems locally using a small-strain formulation: on each time step the solution is obtained in local co-ordinates, which are then updated in the large strain mode.

Solution of equation 5 provides velocities at mesh points used for computation of element strains and of heat advection $\mathbf{u}\nabla T$. These strains are used in equation 6 to calculate element stresses, and the equivalent forces are used to compute velocities for the next time step.

All rheological terms are implemented explicitly. The rheology model is serial viscous–elastic–plastic (Fig. 1a, right, Table 2). The plastic term is given by explicit Mohr–Coulomb plasticity (non-associative, zero dilatency angle) with linear Navier–Coulomb criterion that implies an internal friction angle ϕ of 30° and maximal cohesion S of 20 MPa to fit the experimental Byerlee's law of rock failure (Byerlee 1978):

$$\tau = S + \sigma_n tg\phi$$

where τ is the shear stress and σ_n is the normal stress. In addition, linear cohesion softening is used for better localization of plastic deformation, ε_p, $(S(\varepsilon_p) = S_0 \min(0, 1 - \varepsilon_p/\varepsilon_{p0})$, where ε_{p0} is 0.01).

The ductile–viscous term is represented by non-linear power law with three sets of material parameters (Table 2) that correspond to the properties of the respective lithological layers: upper crust (quartz), middle–lower crust (quartz–diorite), mantle (olivine):

$$\mu_{\mathrm{eff}} = e_{\|}^{\mathrm{d}(1-n)/n}(A^*)^{-1/n}\exp(H/nRT)$$

where $e_{\|}^{\mathrm{d}} = (\mathrm{Inv}_{\|}(e_{ij}))^{1/2}$ is the effective strain rate and $A^* = 1/2A \cdot 3^{(n+1)/2}$ is the material constant, H is the activation enthalpy, R is the gas constant and n is the power-law exponent (Table 2).

The elastic parameters (Table 2) correspond to commonly inferred values from Turcotte & Schubert (2002).

The reference density of the mantle lithosphere is 3330 kg/m^{-3}. The density of the asthenosphere has been varied from 3310 to 3330 kg m^{-3}.

Experiments and results

Figures 3–6 summarize the results of numerical experiments. We have conducted several sets of experiments aimed at testing the influence of the extension rate and of the density structure on the interplay between the gravitational instabilities and tectonically induced deformation.

The extension rate u_x has been varied from 5 to 15 mm year^{-1} at both sides of the system. The chemical density contrast between the mantle and the asthenosphere varied from 0 to 20 kg m^{-3}. For the experiments, we imposed a bilayer crustal structure that corresponds to a granite (quartz-dominated) upper crust with density of 2800 kg m^{-3} and a diabase lower crust with density of 2980 kg m^{-3} (Figs 1a & 2, Tables 1 and 2). The influence of the extension rate, the rheology and the density contrast is characterized by a single non-dimensional parameter, Deborah number (*De*, equation 4). Yet, owing to the depth and laterally variable viscosity, the estimated Deborah number *De* is highly approximate. It is computed from averaged viscosity for 300 km of extension.

De = *0.3–0.75, slow spreading rate* (u_x = *2 × 5 mm year*$^{-1}$)

The results of the experiments at $u_x = 5$ mm year^{-1} and $\Delta\rho = 20$ kg m^{-3} are shown in Figure 3. This case is characterized by development of gravitational instabilities at 1–2 Ma and wide rifting, prior to pronounced narrow rifting, occurring after 6–7 Ma. After this time the mantle lithosphere continues to be thinned by gravitational de-blobbing concurrently with the formation of a rift basin. At $\beta = 5$ (time 6–7 Ma) the rift structure becomes strongly asymmetric and small interior basins form at the backside of one (or both) of the rift flanks. The rift asymmetry appears to be controlled by the gravitational instabilities that have different growth rates on opposite sides of the rift. As mantle viscosity is exponentially dependent on temperature, this asymmetry is reinforced due to viscosity variations caused by asymmetry in the thermal field that also results from the gravitational instabilities.

De = *0.75–1.5, intermediate spreading rate* (u_x = *2 × 10 mm year*$^{-1}$)

The series of experiments at $u_x = 10$ mm year^{-1} and $\Delta\rho = 20$ kg m^{-3} are shown in Figure 4. As in the previous case, mantle instabilities develop at about 2 Ma after the onset of rifting. The mantle lithosphere is broken after 4–5 Ma of rifting. The main features of this case resume to: (1) more pronounced interior basins; (2) ridge-like geometry of the oceanized lithosphere with characteristic ridge-like increase of the depth to the isotherm of 550–600 °C with distance from the centre; and (3) important asymmetry of the margins.

As in the previous case, there is a sharp transition from highly thinned (2–6 km thick) continental crust and mantle lithosphere across the margin to nearly an undeformed zone on the backside of the rift flanks. This sharp transition results from mechanical coupling of the mechanical layers in the rifted zone and from replacement of the weak continental crust by strong oceanized asthenosphere.

There are two major factors defining formation of the interior basins: tensional and gravitational instabilities. For example, high tensile stresses due to faster extension rate and mechanical coupling of the crustal and mantle layers below the rift flanks locally increase the plate strength and thus favour extension in a new place. At slow extension rates ($<2 \times 5$ mm year^{-1}) gravitational instabilities are more efficient. Tensional instabilities are efficient at high extension rate, which appears to be the case of this experiment, compared to the previous experiment. There are, of course, some intermediate situations when the role of both mechanisms is comparable.

De = *1.5–10, high spreading rate* (u_x = *2 × 15 mm year*$^{-1}$)

Figure 5 summarizes the results of the experiments at $u_x = 15$ mm year^{-1} for three values of $\Delta\rho$ (0, 10 and 20 kg m^{-3}). In all cases, the continental lithosphere is already broken up at 3 Ma after the onset of the extension (coefficient of extension, $\beta \approx 4$–5). At 5.6 Ma mantle, upper and lower crust are widely exhumed at the surface (as it is actually observed, for example, beneath the Iberia Abyssal Plain: Whitmarsh *et al.* 2000). In case of zero and weak (10 kg m^{-3}) density contrast (Fig. 5a, b) the interior basins are less pronounced. In the case of higher density contrast (20 kg m^{-3}, Fig. 5c), secondary interior basins develop at rifted margins starting from 5 Ma and form a characteristic structure that resembles that of the rifted continental margins such as the conjugated Iberian and Newfoundland margins (Fig. 6). As discussed above, formation of the interior basins is obviously related to either tensional and/or gravitational instabilities (for extension rates of more than 2×15 mm year^{-1} tensional instabilities dominate) and to the local mechanical coupling between the crustal and mantle layers. This coupling results from

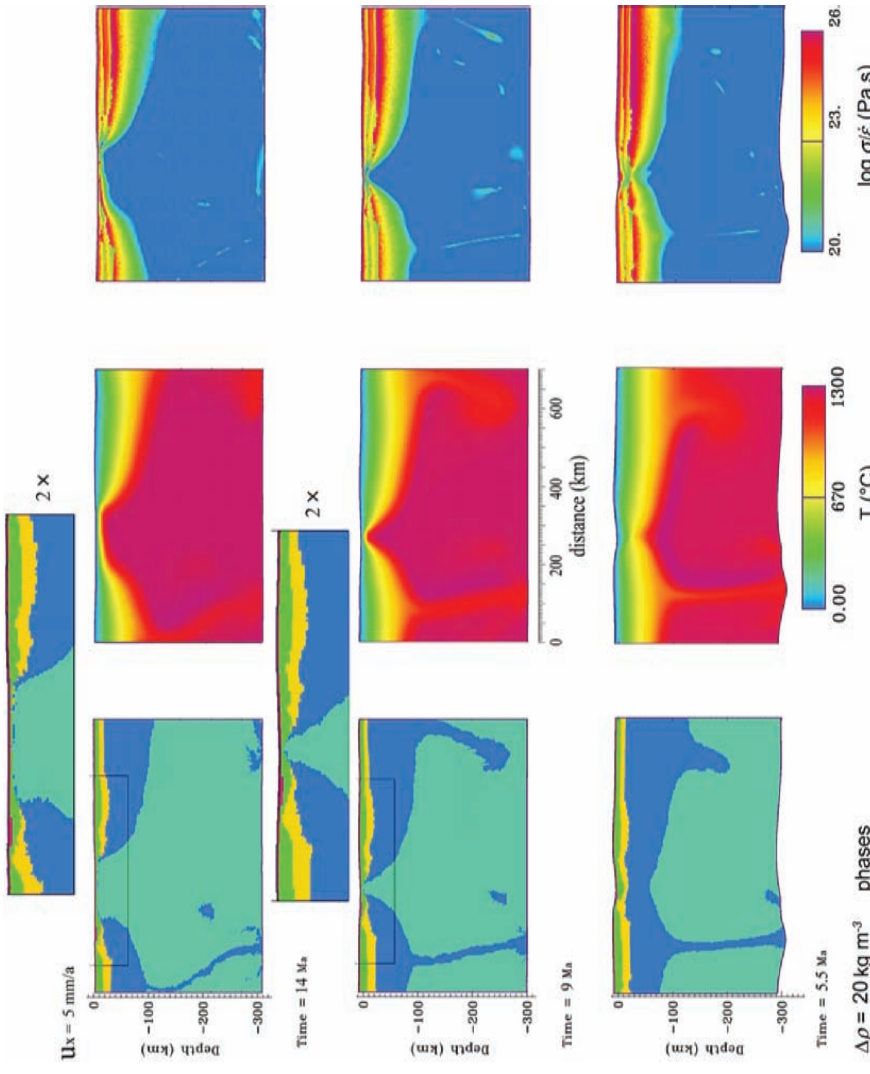


Fig. 3. Results of the experiments for slow extension rate ($u_x = 2 \times 5$ mm year^{-1}) and density contrast between the mantle and asthenosphere $\Delta\rho = 20$ kg m^{-3}. Left: evolution of the material field (colour code: upper crust, salad-green; middle–lower crust, yellow; mantle lithosphere, blue; asthenosphere, marine-green; synrift sediment or otherwise reworked material, purple). Centre: temperature field. Left: logarithm of stress to strain ratio (Pa s), which is equivalent to the effective viscosity for the ductile domains. Note: (1) removal of a large part of the mantle lithosphere by RT instabilities leading to change of style of rifting; (2) strong asymmetric rifting at developed stages of extension; (3) breakup and oceanization of the lithosphere that commences at 9 Ma and is preceded by coupling of the crustal and mechanical layers within the lithosphere; (4) exhumation of small amounts of lower crust and mantle. Arrows show the position of the interior basins. Inserts correspond to ×2 blow-ups of the framed areas. Purple (reworked) material most often directly overlies its source material, i.e. purple above the green layer means material is reworked from the upper crust. Purple above blue means either reworked mantle or sediment derived from the upper and lower crust.

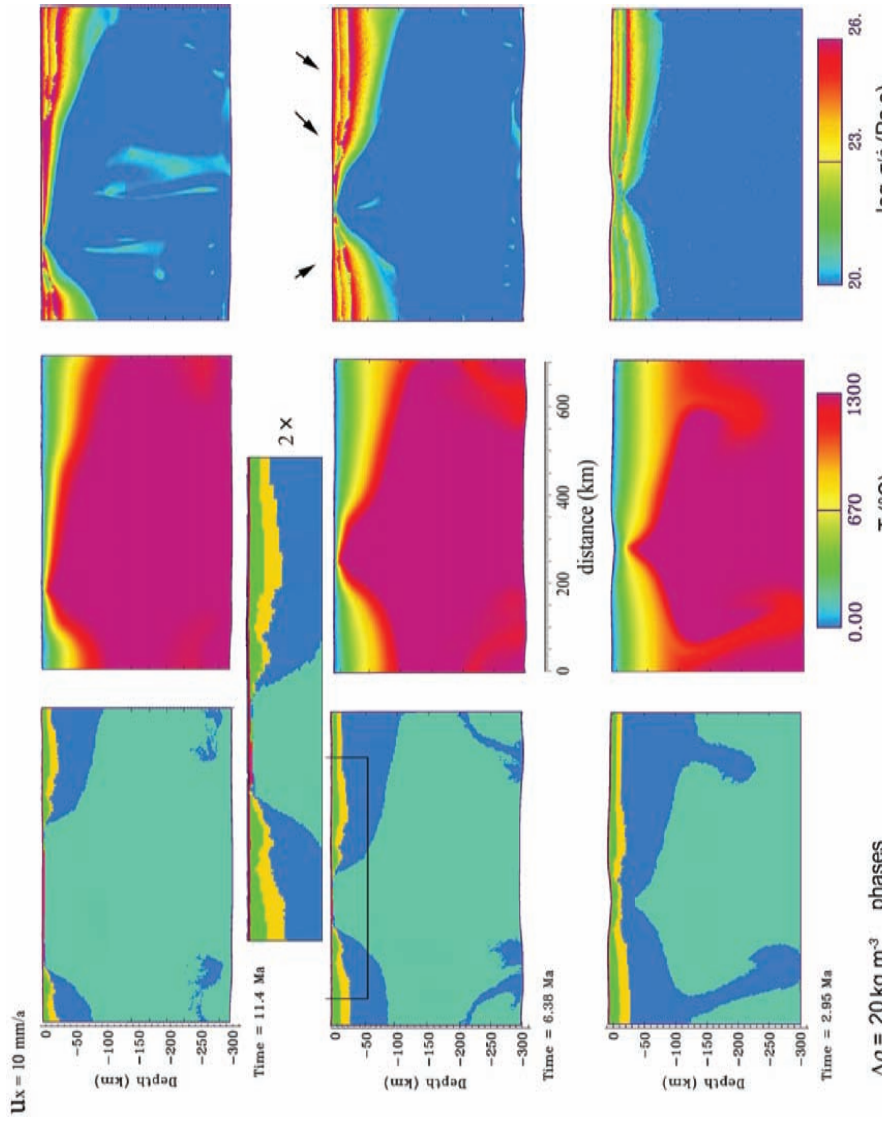


Fig. 4. Results of the experiments for $u_x = 2 \times 10$ mm year^{-1} and $\Delta\rho = 20$ kg m^{-3}. See the caption to Figure 3 for notations. Note: (1) removal of a large part of the mantle lithosphere by RT instabilities leading to change of style of rifting; (2) strong asymmetric rifting at developed stages of extension (at the oceanization stage); and (3) exhumation of continental and oceanic mantle, and punctual exhumation of lower crustal material at ocean–continent limits. In this experiment, continental breakup and oceanization commence at 6 Ma. Arrows show the position of the interior basins. See the description of Figure 3 for other details.

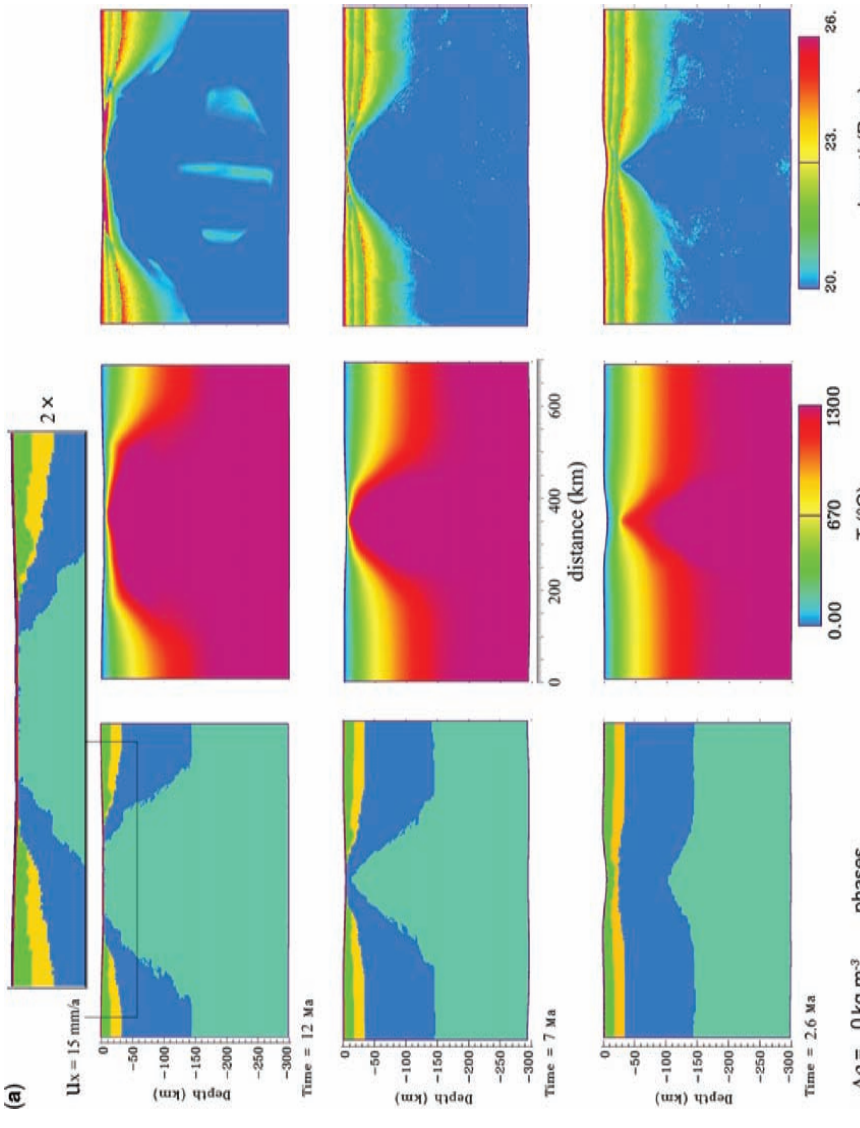


Fig. 5. (**a**) Results of the experiments for $u_x = 2 \times 15$ mm year^{-1} and $\Delta\rho = 0$ kg m^{-3}. See the caption to Figure 3 for other notations. Note: (1) mitigated RT instabilities; (2) nearly symmetric rifting until developed stages of extension (oceanization stage); (3) less expressed interior basins; and (4) exhumation of continental and oceanic mantle, and exhumation of lower crustal material at ocean–continent limits. In this experiment, continental breakup and oceanization commence at 4–5 Ma. See the description of Figure 3 for other details.

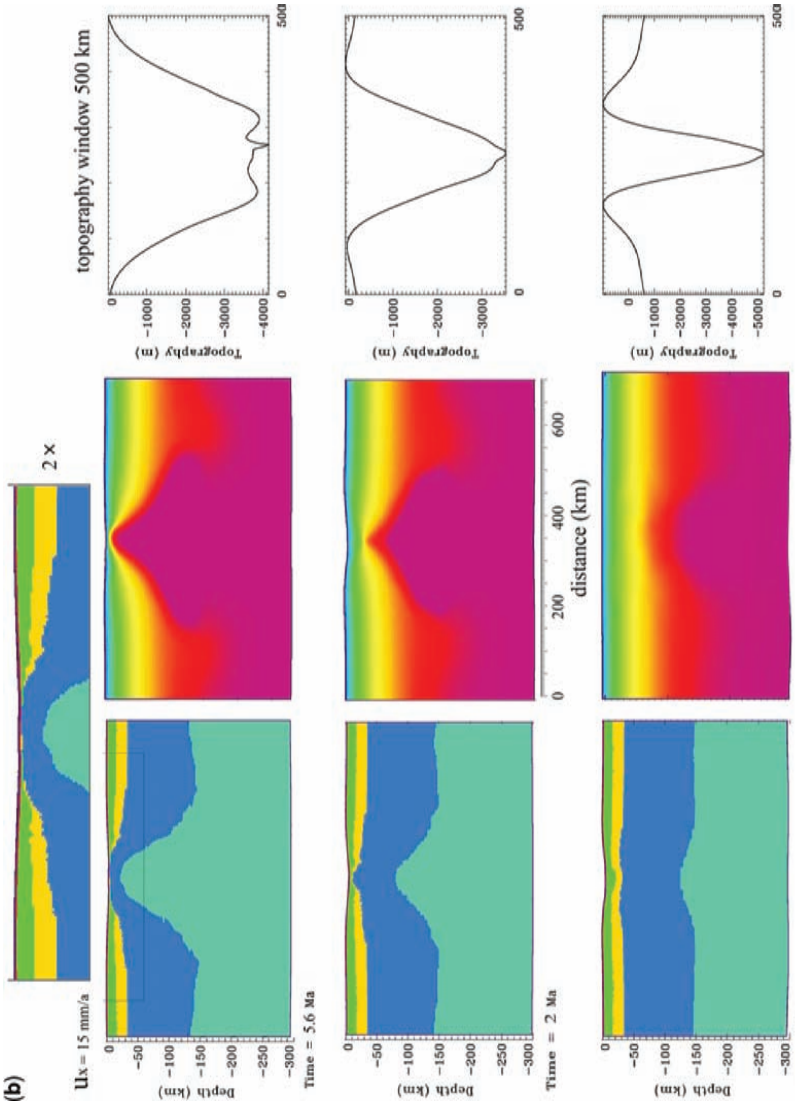


Fig. 5. **(b)** Results of the experiments for $u_x = 2 \times 15$ mm year^{-1} and $\Delta\rho = 10$ kg m^{-3}. Right: topography profiles. See the caption to Figure 3 for other notations. Note: (1) RT instabilities play a remarkable role, starting from 5 Ma; (2) nearly symmetric rifting; and (3) exhumation of continental and oceanic mantle, and exhumation of lower crustal material at ocean–continent limits. In this experiment, continental breakup and oceanization commence at 4–5 Ma. See the description of Figure 3 for other details.

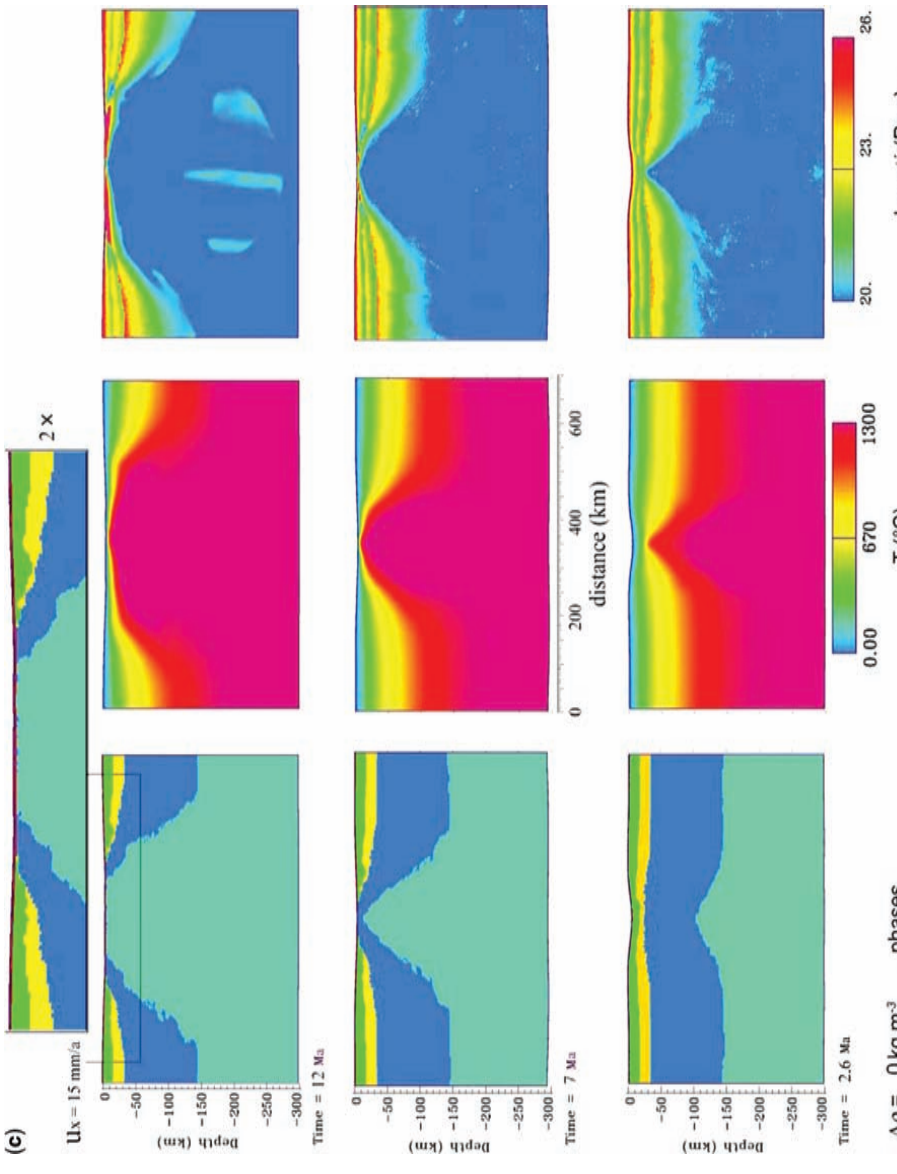
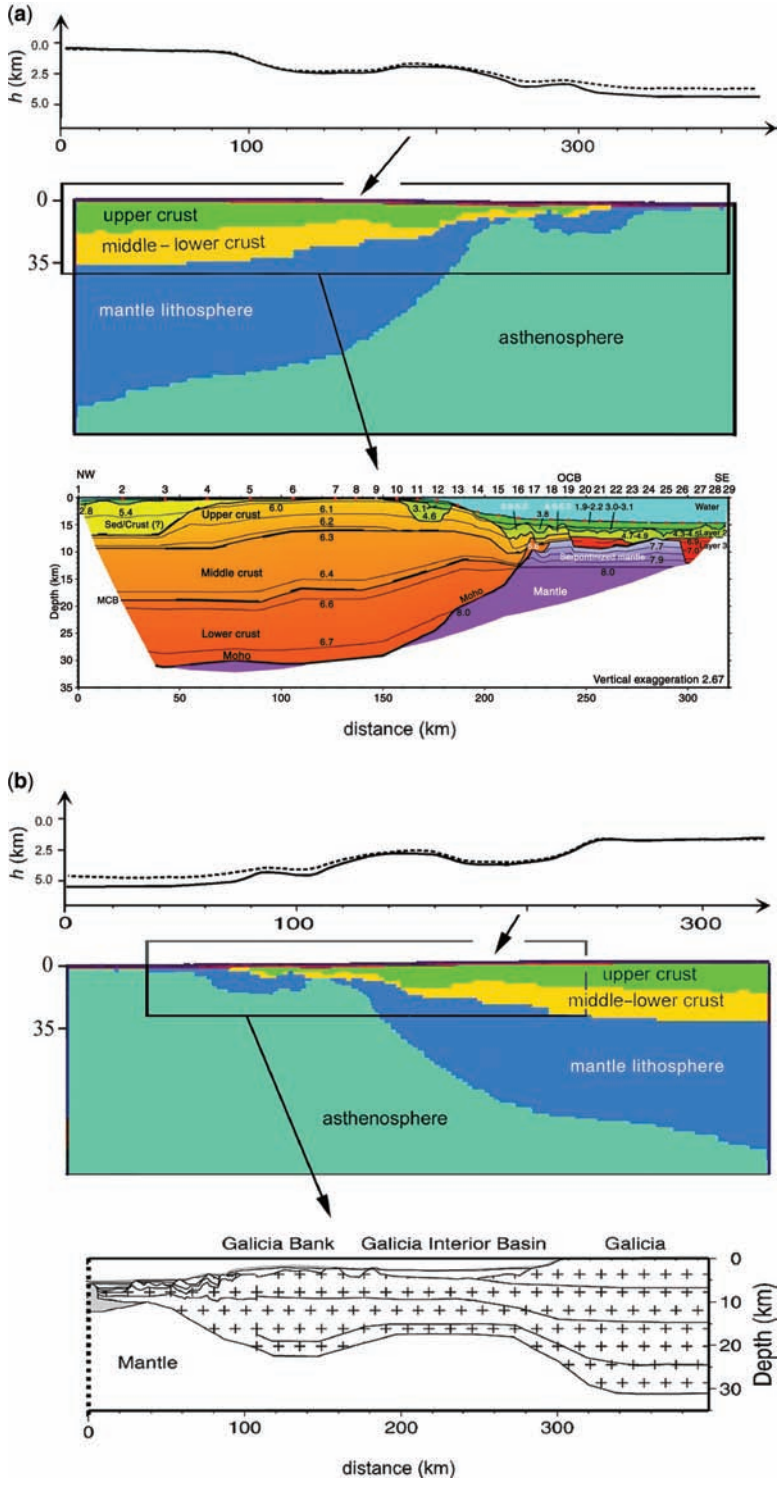


Fig. 5. (c) Results of the experiments for $u_x = 2 \times 15$ mm year^{-1} and $\Delta\rho = 20$ kg m^{-3}. See the caption to Figure 3 for other notations. Note: (1) RT instabilities below the rift flanks play an important role, starting from 2 Ma; (2) unstable extension leading to the formation of boudinage-like structures and interior basins; (3) nearly symmetric rifting; (4) formation of a strong segmented core in the middle of the rift separated by interior basins from the margin; and (5) exhumation of continental and oceanic mantle, and exhumation of lower crustal material at ocean–continent limits. At final tages remnants of the continental crust and mantle are spread in a thin layer (2–6 km thick) over a wide area, some of them being replaced with oceanic material. In this experiment, continental breakup and oceanization commence at 2–3 Ma. Arrows show the position of the interior basins. See the description of Figure 3 for other details.


(a)
h (km)
0.0
2.5
5.0
0
100
300
upper crust
middle – lower crust
mantle lithosphere
asthenosphere
NW
OCB
SE
Sed/Crust (?)
Upper crust
Middle crust
Lower crust
Moho
MCB
Mantle
Water
Depth (km)
Vertical exaggeration 2.67
distance (km)
(b)
h (km)
upper crust
middle–lower crust
mantle lithosphere
asthenosphere
Galicia Bank
Galicia Interior Basin
Galicia
Mantle
Depth (km)
distance (km)

differential thinning accompanied by expulsion (squeezing) of the ductile crust from the thinned zones. As a result, the competent cores of mantle and crustal layers join together. This mechanical coupling locally increases the integrated strength of the lithosphere by a factor of 2 (e.g. Burov & Poliakov 2001), which favours thinning outside of the 'hardened' coupled zone.

For higher extension rate, the rift structure is more symmetric both in the case of low- and high-density contrast (Fig. 5a, b). This confirms the idea that high extension rate reduces the impact of gravity instabilities on the rift asymmetry. In the case of $\Delta\rho = 20\ \mathrm{kg\ m^{-3}}$ (Fig. 5c) the vertical amplitude of gravity instability in the mantle part becomes important and reaches 20–50 km after only 2 Ma of rifting. The lithosphere under both rift flanks thickens, leaving a narrowing stretched zone in between, which obviously helps to switch rifting from wide mode to narrow mode. The instability continues to develop at the exponential rate leading to de-blobbing of a part of the lithospheric mantle at the depth level corresponding to the effective viscosity of about 10^{21} Pa s (Fig. 5c). After this moment the mantle below the rift flanks is removed. The whole system remains roughly symmetric, with similar interior basins formed on both sides of the rift. Figure 6 compares the results of the experiment for $\Delta\rho = 20\ \mathrm{kg\ m^{-3}}$ with the present-day structure of the conjugated rifted margins of Flemish Cap and Galicia (Funck *et al.* 2003). It reveals a number of important similarities: the geometry of the extended zones, the sharp transition from the extremely stretched crust and mantle to practically underformed lithosphere (e.g. the Flemish Cap), the geometry of the exhumed mantle and that of the exhumed lower crustal zones (e.g. Whitmarsh *et al.* 2000), the geometry and wavelength of the interior basins (Fig. 6b) (Galicia Interior Basin: Pérez-Gussinyé *et al.* 2003). Even though the partial melting is not included in the present experiments, there is no difficulty in predicting, when examining Figures 5c, & 6a, b, the location of the potential zones of partial melting that are seemingly compatible with those interpreted from the seismic cross-sections (Funck *et al.* 2003).

Discussion and conclusions

- The experiments demonstrate the importance of the negative RT instabilities during the formation of 'slow' margins and continental rifts. These instabilities are highly effective in the range of $0 < De < 10$, or in the range of initial spreading velocities $0–2 \times 15\ \mathrm{mm\ year^{-1}}$. The RT instabilities are most efficient for $De \leq 1$ and spreading rates $\leq 2 \times 10\ \mathrm{mm\ year^{-1}}$. The instabilities largely control rift symmetry and rifting mode. For example, the transfer from wide to narrow rift mode for $De < 3$ or $u_x \leq 2 \times 15\ \mathrm{mm\ year^{-1}}$ may be associated with gravitational thinning and localized downwelling of the mantle lithosphere. In the absence of specific mechanisms of softening or inherited structures, rift asymmetry may result from gravitational instabilities and differential stretching for $De < 1$ or $u_x < 2 \times 10\ \mathrm{mm\ year^{-1}}$. As the temperature dependence of both the viscosity and the growth rate of instabilities is exponential, a minor variation in the thickness of lithospheric layers results in asymmetric rifting in case of small extension rates. Extension at rates of less than $2 \times 5\ \mathrm{mm\ year^{-1}}$ produces highly unstable asymmetric rifting.
- Formation of the interior basins at rifted margins, such as the Galicia Interior Basin (e.g. Pérez-Gussinyé *et al.* 2003), may be linked to the interplay between the tensional and gravitational instabilities and local mechanical coupling–uncoupling of the intracrustal and mantle layers for $De < 10$ and $\beta > 4–5$. At slow spreading

Fig. 6. (**a**) Comparison of the results of the experiment shown in Figure 5c ($u_x = 15\ \mathrm{mm\ year^{-1}}$, $\Delta\rho = 20\ \mathrm{kg\ m^{-3}}$) with the present-day structure of the Flemish Cap margin (Funck *et al.* 2003). Note the similarities in the sharp transition from the deformed to undeformed continental lithosphere in the geometry of the extended crustal blocks including exhumed lower crustal and mantle material. Note that the actual margin has experienced major thermal subsidence and probably additional extension or other deformation after the rifting phase. Arrows show the position of the interior basins. The dashed line on the topography plot corresponds to the basement before water loading. See the description of Figure 3 for other details. (**b**) Comparison of the results of the experiment shown in Figure 5c ($u_x = 15\ \mathrm{mm\ year^{-1}}$, $\Delta\rho = 20\ \mathrm{kg\ m^{-3}}$) with the actual structure of the Galicia margin that is conjugated with the Flemish Cap margin (Funck *et al.* 2003). Note the similarities in the geometry of the interior basins, in sharp transition from deformed thinned crust and mantle to undeformed continental lithosphere, in the geometry of the extended crustal blocks including exhumed lower crust and mantle material. Numerical resolution does not allow localized faulting to be reproduced, but comparison with Tirel *et al.* 2004 (based on the same numerical code) suggests that detachment faults appear in the zones of extra-thinned crust. Note that the actual margin has experienced major thermal subsidence and probably additional extension or other deformation after the rifting phase. Arrows show the position of the interior basins. The dashed line on the topography plot corresponds to the basement before water loading. See the description of Figure 3 for other details.

rates (2×10 mm year^{-1}), gravity-driven instabilities dominate and generate interior basins for chemical density contrasts greater than 10 kg m^{-3}. At higher extension rates, interior basins are amplified by tensional instabilities, even for small compositional density contrasts. Prebreakup thinning of the crust and mantle first results in weakening of the continental lithosphere. Yet, in later stages ($\beta > 4-5$) it leads to localized mechanical coupling of the competent crustal and mantle layers below the rift flanks, which locally increases the integrated strength of the lithosphere (e.g. Burov & Diament 1995). As a result, the interior zones (interior basins) become relatively weaker than the zones of mechanical coupling, and become a subject of more important stretching than the coupled zones.

- The experiments for 'high' extension rate (2×15 mm year^{-1}) and $\Delta\rho = 20$ kg m^{-3} (Figs 5c & 6) demonstrate important similarities with the observations (Funck *et al.* 2003). In particular, the predicted geometry of sharp transition from zones of highly stretched crust (1–6 km thick) to practically undeformed crust and lithosphere below the rift flanks resembles that of the Flemish Cap and Galicia margin. The model predicts that the extension of the continental crust may occur in an extremely wide zone. In particular, after 9 Ma, $\beta = 5-15$, the continental crust (Figs 5c & 6) thins from 30–40 km to only 1–2 km over a 80–100 km-wide zone across the modelled margin. This crust is then punctually or totally replaced with the new oceanic material. The uplifted/exhumed mantle underlies (depth of less than 2–5 km below the bottom) or directly replaces the ultra-thinned continental and oceanic material over a 70–100 km-wide continent–ocean transition zone (e.g. Fig. 6a). The wide zones of extended continental crust (stretched to a less than 5–6 km-thick layer) produced in the model are indeed observed across the Galicia margin. The model predicts important exhumation of the continental mantle and punctual exhumation of the lower crust, in between the exhumed upper crust and mantle. In the case of instable extension, this crust may periodically alternate with the mantle (e.g. serpentinized) and the upper crustal material. The predicted vertical crustal undulations resulting from gravitational and tensional instabilities may be associated with prominent detachment faulting, as was shown (using same numerical code) for domal uplift instabilities in Tirel *et al.* (2004). Yet, the numerical resolution of the present model is insufficient to reproduce localized faulting. However, the predicted patterns of accumulated plastic strain suggest that stretched and undulated upper crust deforms along the detachment faults across the margin. In the model, interior basins are formed either on both sides of the rift (high extension rate of 2×15 mm year^{-1}) or only on one side (specifically for smaller extension rates $<2 \times 10$ mm year^{-1}). This process is governed by gravitational and tensional instabilities in multilayered lithosphere.
- The experiments show that it is more difficult, although not impossible, to reproduce final structure of 'slow' rifted margins under assumption of low extension rates (<5 mm year^{-1}) during the entire duration of the phase. In particular, slow extension rates ($<2 \times 10$ mm year^{-1}) are associated with unstable asymmetric rifting, whereas the conjugated slow margins such as the Flemish Cap–Galicia margin demonstrate less asymmetry than could be expected from the models, for reported extension rates of less than 5 mm year^{-1}. Consequently, it is not excluded that the extension rate could be higher at some prebreakup stages of rifting, and then slows down later to yield the reported average rate of 5 mm year^{-1}. This does not, of course, exclude the possibility that the extension rate could increase after the breakup. Indeed, most reliable (magnetic) data refer to sea-floor spreading stage after continental breakup (e.g. Srivastava *et al.* 2000). The extension rate at the prebreakup stage is much less constrained. One can admit that rift systems are subject to large prebreakup variations of the extension rate. This may explain the multitude of rifting styles even for comparable average spreading rates and coefficients of extension β. An alternative explanation may infer smaller density contrasts or stronger ductile rheology. Yet, in this case the formation of interior basins will be less probable.
- It is necessary to stress the primary importance of obtaining better constraints on the major parameters controlling margin evolution: (1) the compositional density contrast between the mantle and asthenosphere; (2) the prerift thermo-rheological structure; and (3) the extension rate as a function of time. These parameters are difficult to derive from the available data, and their acquisition presents a new challenge for future geological and geophysical exploration of continental margins.
- Of course, the results for narrow and wide rift might infer different reaction in terms of developing instability. We here have exploited only those initial geometrical and thermal configurations that represent in some way Flemish Cap–Galicia margins. The configurations, however, look to be quite generally applicable to slow extension zones.

The author thanks the reviewers – R. Govers, L. Moresi and M. Pérez-Gussinyé – for highly constructive comments. I also thank G. Karner and the organizers of the IMEDL workshop for the invitation to participate and the following inspiring discussions. The numerical code Par(a)ovoz v.9 is a product of Paravoz v.3 (1996) by Poliakov and Podladchikov (Poliakov *et al.* 1993). This study has benefited from partial support by the MEBE program.

References

BASSI, G. 1995. Relative importance of strain rate and rheology for the mode of continental extension. *Geophysical Journal International*, **122**, 195–210.

BASSI, G. & BONNIN, J. 1988. Rheological modeling and deformation instability of lithosphere under extension. *Geophysical Journal International*, **93**, 485–504.

BOTT, M. H. P. 1971. Evolution of young continental margins. *Tectonophysics*, **11**, 319–327.

BUCK, W. R. 1991. Modes of continental lithospheric extension. *Journal of Geophysical Research*, **96**, 20,161–20,178.

BUCK, W. R. & POLIAKOV, A. N. B. 1998. Abyssal hills formed by stretching oceanic lithosphere. *Nature*, **392**, 272–275.

BUROV, E. B. & CLOETINGH, S. 1997. Erosion and rift dynamics: new thermomechanical aspects of post-rift evolution of extensional basins. *Earth and Planetary Science Letters*, **150**, 7–26.

BUROV, E. B. & DIAMENT, M. 1995. The effective elastic thickness (Te) of continental lithosphere: What does it really mean? *Journal of Geophysical Research*, **100**, 3895–3904.

BUROV, E. B. & POLIAKOV, A. N. B. 2001. Erosion and rheology controls on synrift and postrift evolution: Verifying old and new ideas using a fully coupled numerical model. *Journal of Geophysical Research*, **106**, 16,461–16,481.

BUROV, E. & POLIAKOV, A. 2003. Erosional forcing on basin dynamics: new aspects of syn- and post-rift evolution. *In*: NIEUWLAND, D. A. (ed.) *New Insights into Structural Interpretation and Modelling*. Geological Society, London, Special Publications, **212**, 209–224.

BYERLEE, J. D. 1978. Friction of rocks. *Pure & Applied Geophysics*, **116**, 615–626.

CHANDRASEKHAR, S. 1961. *Hydrodynamic and Hydromagnetic Stability.* Oxford University Press.

CLOETINGH, S. A. P. L., WORTEL, M. J. R. & VLAAR, N. J. 1982. Evolution of passive continental margins and initiation of subduction zones. *Nature*, **297**, 139–142.

CONRAD, C. P. & MOLNAR, P. 1999. Convective instability of a boundary layer with temperature and strain-rate-dependent viscosity in terms of 'available buoyancy'. *Geophysical Journal International*, **139**, 51–68.

CUNDALL, P. A. 1989. Numerical experiments on localization in frictional materials. *Ingenieur-Archiv*, **59**, 148–159.

DUNBAR, J. A. & SAWYER, D. S. 1988. Continental rifting at pre-existing lithospheric weakness. *Nature*, **333**, 450–452.

HOPPER, J. R., FUNCK, T. *ET AL.* 2004. Continental breakup and the onset of ultraslow seafloor off Flemish Cap on the Newfoundland rifted margin. *Geology*, **32**, 93–96.

HOUSEMAN, G. A. & MOLNAR, P. 1997. Gravitational (Rayleigh–Taylor) instability of a layer with non-linear viscosity and convergence thinning of continental lithosphere. *Geophysical Journal International*, **128**, 125–150.

HOUSEMAN, G. A., MCKENZIE, D. P. & MOLNAR, P. 1981. Convective instability of a thickened boundary layer and its relevance for the thermal evolution of continental convergent belts. *Journal of Geophysical Research*, **86**, 6135–6155.

HUISMANS, R. S. & BEAUMONT, C. 2007. Roles of lithospheric strain softening and heterogeneity in determining the geometry of rifts and continental margins. *In*: KARNER, G. D., MANATSCHAL, G. & PINHEIRO, L. M. (eds) *Imaging, Mapping and Modelling Continental Lithosphere Extension and Breakup*. Geological Society, London, Special Publications, **282**, 111–138.

HUISMANS, R. S., PODLADCHIKOV, Y. Y. & CLOETINGH, S. 1998. The transition from passive to active rifting, relative importance of asthenospheric doming and passive extension of the lithosphere. *Journal of Geophysical Research*, **106**(B6), 11271–11292.

FLETCHER, R. C. & HALLET, B. 1983. Unstable extension of the lithosphere: A mechanical model for Basin-and-Range structure. *Journal of Geophysical Research*, **88**, 7457–7466.

FUNCK, T., HOPPER, J. R., LARSEN, H. C., LOUDEN, K. E., TUCHOLKE, B. E. & HOLBROOK, W. S. 2003. Crustal structure of the ocean–continent transition at Flemish Cap: Seismic refraction results. *Journal of Geophysical Research*, **108**(B11), 2531, doi:10.1029/2003JB002434.

JAUPART, C. & MARESCHAL, J. C. 1999. The thermal structure and thickness of continental roots. *Lithos*, **48**, 93–114.

KEEN, C. E. & BOUTILIER, R. R. 1995. Lithosphere–asthenosphere interactions below rifts. *In*: BANDA, E. (ed.) *Rifted Ocean–Continent Boundaries*. Kluwer, Norwell, MA, 17–30.

KIRBY, S. H. & KRONENBERG, A. K. 1987. Rheology of the lithosphere: Selected topics. *Reviews of Geophysics*, **25**, 1219–1244.

KOHLSTEDT, D. L., EVANS, B. & MACKWELL, S. J. 1995. Strength of the lithosphere: Constraints imposed by laboratory experiments. *Journal of Geophysical Research*, **100**, 17587–17602.

KUSZNIR, N. & KARNER, G. 1985. Dependence of the flexural rigidity of the continental lithosphere on rheology and temperature. *Nature*, **316**, 138–142.

LAVIER, L. L., BUCK, W. R. & POLIAKOV, A. N. B. 2000. Factors controlling normal fault offset in ideal brittle layer. *Journal of Geophysical Research*, **105**, 23431–23442.

LE POURHIET, L., BUROV, E. & MORETTI, I. 2004. Rifting through a stack of inhomogeneous thrusts (the dipping pie concept). *Tectonics*, **23**, TC4005, doi:10.1029/2003TC001584.

MANATSCHAL, G. 2004. New models for evolution of magma-poor rifted margins based on the review of data and concepts from West Iberia and the Alps. *International Journal of Earth Sciences*, **93**, 432–466.

MANATSCHAL, G. & BERNOULLI, D. 1999. Architecture and tectonic evolution of nonvolcanic margins: Present-day Galicia and ancient Adria. *Tectonics*, **6**, 1099–1119.

MANATSCHAL, G., FROITZHEIM, N., RUBENACH, M. & TURRIN, B. D. 2001. The role of detachment faulting in the formation of an ocean–continent transition: insights from the Iberia Abyssal Plain. *In*: WILSON, R. C. L., WHITMARSH, R. B., TAYLOR, B. & FROITZHEIM, N. (eds) *Non-volcanic Rifting of Continental Margins: A Comparison of Evidence from Land and Sea*. Geological Society, London, Special Publications, **187**, 405–428.

MCKENZIE, D. 1978. Some remarks on the development of sedimentary basins. *Earth and Planetary Science Letters*, **40**, 25–32.

PÉREZ-GUSSINYÉ, M., RESTON, T. J. & MORGAN, J. P. 2001. Serpentinisation and magmatism at non-volcanic margins – The effect of the initial lithospheric structure. *In*: WILSON, R. C. L., WHITMARSH, R. B., TAYLOR, B. & FROITZHEIM, N. (eds) *Non-volcanic Rifting of Continental Margins: A Comparison of Evidence From Land and Sea*. Geological Society, London, Special Publications, **187**, 551–576.

PÉREZ-GUSSINYÉ, M., RANERO, C. R. & RESTON, T. J. 2003. Mechanisms of extension at nonvolcanic margins: evidence from the Galicia interior basin, west of Iberia. *Journal of Geophysical Research*, **108**(B5), 2245, doi:10.1029/2001JB000901.

POLIAKOV, A. N. B., PODLADCHIKOV, YU. & TALBOT, C. 1993. Initiation of salt diapirs with frictional overburden: numerical experiments. *Tectonophysics*, **228**, 199–210.

ROYDEN, L. & KEEN, C. E. 1980. Rifting process and thermal evolution of the continental margin of Eastern Canada determined from subsidence curves. *Earth and Planetary Science Letters*, **51**, 343–361.

POUDJOM DJOMANI, Y. H., O'REILLY, S. Y., GRIFFIN, W. L. & MORGAN, P. 2001. The density structure of subcontinental lithosphere: Constraints on delamination models. *Earth and Planetary Science Letters*, **184**, 605–621.

O'REILLY, S. Y., GRIFFIN, W. L., POUDJOM DJOMANI, Y. & MORGAN, P. 2001. Are lithospheres forever? Tracking changes in subcontinental lithospheric mantle through time. *GSA Today*, **11**, 469.

SALVENSON, J. O. 1978. Variations in the geology of rift basins; a tectonic model. *Conference Proceedings of Los Alamos Scientific Laboratory*, **7487**, 82–86.

SRIVASTAVA, S. P., SIBUET, J.-C., CANDE, S., ROEST, W. R. & REID, I. D. 2000. Magnetic evidence for slow seafloor spreading during the formation of the Newfoundland and Iberian margins. *Earth and Planetary Science Letters*, **182**, 61–76.

STACEY, F. D. 1992. *Physics of the Earth*. Brookfield Press, Brisbane.

STEPHENSON, R. A., NAKIBOGLU, S. M. & KELLY, M. A. 1989. Effects of astenosphere melting, regional thermoisostasy, and sediment loading on the thermomechanical subsidence of extensional sedimentary basins. *In*: PRICE, R. A. (ed.) *Origin and Evolution of Sedimentary Basins and their Energy and Mineral Resources*. American Geophysical Union, Geophysical Monograph, **48**, 17–27.

TIREL, C., BRUN, J.-P. & BUROV, E. 2004. Thermomechanical modeling of extensional gneiss dome. *In*: *Gneiss Domes and Orogeny*. Geological Society of America, Special Paper **380**, 67–78.

TURCOTTE, D. L. & SCHUBERT, G. 2002. *Geodynamics*. Cambridge University Press, Cambridge.

WHITMARSH, R. B., DEAN, S. M., MINSHULL, T. A. & TOMPKINS, M. 2000. Tectonic implications of exposure of lower continental crust beneath the Iberia Abyssal Plain, northeast Atlantic Ocean: Geophysical evidence. *Tectonics*, **19**, 919–942.